applied sciences

IMPACT FACTOR 2.5

CITESCORE 5.5

Article

Impact of Non-Linear CT Resampling on Enhancing Synthetic-CT Generation in Total Marrow and Lymphoid Irradiation

Monica Bianchi, Nicola Lambri, Daniele Loiacono, Stefano Tomatis, Marta Scorsetti, Cristina Lenardi and Pietro Mancosu

MDPI

https://doi.org/10.3390/app16031660

applied sciences

MDPI

Article

Impact of Non-Linear CT Resampling on Enhancing Synthetic-CT Generation in Total Marrow and Lymphoid Irradiation

Monica Bianchi [1,2,†], Nicola Lambri [1,3,*,†], Daniele Loiacono [4], Stefano Tomatis [1], Marta Scorsetti [1,5], Cristina Lenardi [2,6] and Pietro Mancosu [1,5]

1 IRCCS Humanitas Research Hospital, Radiotherapy and Radiosurgery Department, via Manzoni 56, 20089 Milan, Italy; monica.bianchi5@studenti.unimi.it (M.B.); stefano.tomatis@humanitas.it (S.T.); marta.scorsetti@hunimed.eu (M.S.); pietro.mancosu@hunimed.eu (P.M.)
2 Dipartimento di Fisica "Aldo Pontremoli", Università degli Studi di Milano, via Giovanni Celoria 16, 20133 Milan, Italy; cristina.lenardi@unimi.it
3 Scuola di Specializzazione in Fisica Medica, Università degli Studi di Milano, via Giovanni Celoria 16, 20133 Milan, Italy
4 Dipartimento di Elettronica, Informazione e Bioingegneria, Politecnico di Milano, via Giuseppe Ponzio 34, 20133 Milan, Italy; daniele.loiacono@polimi.it
5 Department of Biomedical Sciences, Humanitas University, via Rita Levi Montalcini 4, 20072 Milan, Italy
6 INFN, Sezione di Milano, via Giovanni Celoria 16, 20133 Milan, Italy
* Correspondence: nicola.lambri@cancercenter.humanitas.it
† These authors contributed equally to this work.

Abstract

Computed tomography (CT) images are stored at a 12-bit depth. However, many deep learning libraries and pre-trained models are designed for 8-bit images, requiring an intermediate compression step before restoring the original 12-bit physical range. This process causes information loss and can compromise image reliability. This study investigated the impact of two CT resampling methods (8-bit compression; 12-bit decompression) on dose calculation and image quality. Ten total marrow and lymphoid irradiation patients were selected. CT scans were resampled using linear and non-linear look-up tables (l_LUT/nl_LUT). Original and resampled CTs were evaluated considering: (i) Hounsfield unit (HU) root mean squared error (RMSE); (ii) dose-volume histogram (DVH) statistics for target volume and several organs; (iii) 3D gamma passing rate (GPR) with a 1%/1.25 mm criterion; (iv) lymph nodes contouring and diagnostic quality (scale 1–5). The RMSE for l_LUT vs. nl_LUT was 7 ± 1 vs. 10 ± 1 HU. Maximum differences in DVH statistics were 0.4%, with a 3D-GPR = 100% for all cases. CTs resampled with l_LUT exhibited evident brain pixelation (score = 1), whereas nl_LUT matched the original CT quality (score = 4). Both LUTs were acceptable for lymph nodes delineation. The nl_LUT optimized the CT resampling process, providing a more efficient method for possible deep learning applications in synthetic CT generation.

Keywords: image compression; look-up table; synthetic CT; total marrow irradiation (TMI); total marrow and lymphoid irradiation (TMLI)

Check for updates

Academic Editor: Douglas O'Shaughnessy

Received: 29 December 2025
Revised: 26 January 2026
Accepted: 3 February 2026
Published: 6 February 2026

Copyright: © 2026 by the authors. Licensee MDPI, Basel, Switzerland. This article is an open access article distributed under the terms and conditions of the Creative Commons Attribution (CC BY) license.

1. Introduction

Radiation therapy (RT) traditionally relies on computed tomography (CT) to acquire patient images and optimize treatment plans. However, magnetic resonance imaging (MRI) can be more accurate in characterizing soft tissues and visualizing the tumor extent [1–3].

These advantages are particularly valuable in RT planning, aiding in the delineation of target volumes and organs at risk (OARs). Unlike CT, MRI does not provide electron density information, which is essential for dose calculation. Consequently, RT workflows often require the co-registration of CT and MRI to leverage the complementary strengths of both imaging modalities. A similar limitation applies to cone beam computed tomography (CBCT), which holds a crucial role in image-guided adaptive RT. Furthermore, CBCT is affected by artifacts caused by increased scatter and truncated projections, thereby hindering its accuracy for dose calculations [4,5].

Various methods have been proposed to generate synthetic CT (sCT) from MRI or CBCT data to streamline the RT workflow. Recently, considerable efforts have focused on deep learning-based approaches [6–9], and artificial intelligence (AI) algorithms have shown promising results. In particular, recent methods involve the development of models trained using 2.5D inputs (i.e., adjacent slices treated as separate channels) or fully 3D architectures [10–14].

CT images are stored with a 12-bit depth, ranging from −1024 to 3071 Hounsfield units (HU), and are represented in memory in a 16-bit format. However, many deep learning models and libraries for synthetic image generation, segmentation, or other image-processing tasks are designed for 8-bit representations, as is typical for natural images [15]. Consequently, when training deep learning models, CT images are commonly preprocessed by normalizing pixel values prior to conversion to 8-bit format [16]. This process results in a compression of the entire intensity range, causing information loss and potentially compromising image reliability. Moreover, such compression may result in suboptimal performance due to the non-uniform clinical importance of different intensity ranges in CT images. For instance, although the HU range of soft tissues (0–100 HU) accounts for approximately 2% of the total range, soft tissues account for the majority of voxels within the patient's body. As a result, deep learning models for sCT generation may exhibit reduced accuracy when the 8-bit output is mapped back to the original 12-bit HU range required for dose calculation.

In this study, we investigate the effects of a linear and a non-linear approach for 8-bit compression and subsequent 12-bit decompression of CT images. While the former represents a standard method for data normalization, the latter is specifically introduced to improve HU representation in soft tissue regions. Our aim is to quantify the impact of these methods on reconstructed image fidelity and dose calculation accuracy. This analysis constitutes a necessary preliminary step to ensure proper training and use of AI models for sCT generation using the proposed non-linear strategy.

2. Materials and Methods

2.1. Patient Selection

Ten patients treated with total marrow and lymphoid irradiation (TMLI) after 2020 were selected, reflecting the most recent departmental practice for this technique. The extended scan length and large target volume of TMLI enabled the evaluation of the impact of 8-bit compression across a wide range of soft tissue contrasts and tissue densities. As per our internal protocol, the prescribed dose was 2 Gy delivered in a single fraction.

Patients were positioned supine with their arms alongside their body, utilizing a custom-made frame and personalized masks for immobilization [17]. A BigBore CT system (Philips Healthcare, Best, The Netherlands) was used to acquire free-breathing CT scans from head to mid femurs with 5 mm slice thickness. The field of view was set to 60 cm, while the iterative metal artifact reduction (iMAR) algorithm built in the CT was used in exceptional cases [18].

The clinical target volume (CTV) comprised the bone marrow, spleen and lymph node chains, while the planning target volume (PTV) was defined as the union of isotropically expanded CTV to account for setup margin and motion [19]. OARs included lenses, eyes, brain, lungs, heart, kidneys, bowels, stomach, liver, rectum, and bladder.

Treatment plans were optimized by the progressive resolution optimizer (PROIII v13) or the photon optimization (PO v15) algorithms and delivered with a TrueBeam linac (Varian Medical Systems, Palo Alto, CA, USA) employing a volumetric modulated arc therapy (VMAT) technique. Dose calculations utilized the analytical anisotropic algorithm (AAA v11–15). Plan optimization involved a multi-isocenter approach with 5 isocenters and 10 full arcs (360°), overlapping by a minimum of 2 cm to reduce dose distribution uncertainty due to patient setup. The collimator angle was fixed at 90°, with an uneven jaw aperture in the cranial–caudal direction and a maximum aperture of 40 cm in the left–right direction [20].

2.2. CT Resampling

The processing of original CTs (oCTs) involved a compression from 12 to 8 bits, and a subsequent decompression from 8 to 12 bits. Throughout the manuscript, we refer to this procedure as "CT resampling" and to a compressed–decompressed CT as "resampled CT" (rCT). Two compression methods were implemented using a linear and a non-linear look-up table (l_LUT and nl_LUT, respectively), as illustrated in Figure S1 in the Supplementary Material.

The l_LUT applied a naïve mapping of the original HU values to an 8-bit range using a fixed step size of 16 HU. In contrast, the nl_LUT was designed as a piecewise function based on the authors' clinical experience to enhance the representation of soft tissues (see Table 1). The discretization step was refined to 2 HU within the 0–100 HU range, where small density variations are clinically relevant, as shown in Figure 1. Toward the extremities of the HU scale, the step size increased non-linearly, reaching 100 HU for densities above 1650 HU, in order to optimize data compression while preserving the contrast necessary for distinguishing high-density structures.

Table 1. Typical range of HU for tissues and organs and their respective discretization step when compressing the oCT with the nl_LUT.

Tissue or Organ	HU Range	Discretization Step
Lung [21]	−900 to −500	35
Soft tissue	0 to 100	2
Blood [22]	30 to 45	2
Brain [23]	20 to 40	2
Liver [24]	40 to 65	2
Bone [22]	250 to 400	5
	400 to 800	16
	800 to 1200	50

Abbreviations: nl_LUT, non-linear look-up table; oCT, original CT.

2.3. Dose Calculation

Both linearly and non-linearly resampled CTs (l_rCTs and nl_rCTs, respectively) were imported into the Eclipse treatment planning system (v16.1; Varian Medical Systems, Palo Alto, CA, USA). To evaluate the magnitude of errors introduced by resampling in the dose calculation, three treatment plans per patient were recalculated using AAA on oCTs and rCTs. All dose distributions were recalculated under the same conditions with respect to the clinical plans, i.e., equal MUs, structures, prescription, field geometry, leaf sequencing, and grid resolution of 2.5 mm.

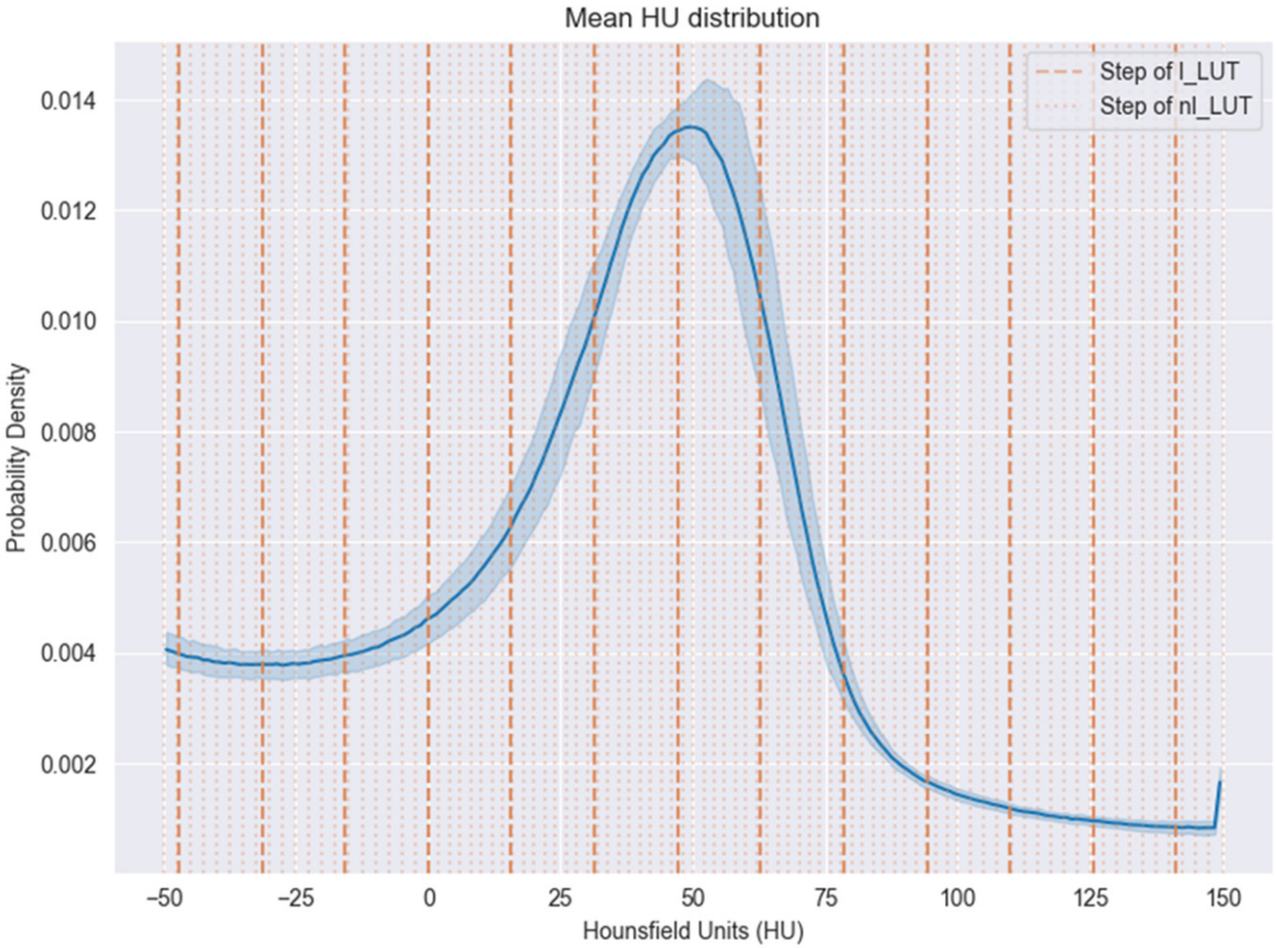

Figure 1. HU distribution in soft tissues across the patient cohort, overlaid with linear (l_LUT) and non-linear (nl_LUT) discretization steps (dashed and dotted vertical lines, respectively). The band shows the 95% CI across the cohort. Abbreviations: CI, confidence interval; l_LUT, linear look-up table; nl_LUT, non-linear look-up table.

2.4. Data Analysis

For each patient, two CT compression methods were used, totaling 30 CT series and 30 dose distributions analyzed. The impact of resampling on the accuracy of HU values was assessed by computing the root mean squared error (RMSE) between oCTs and rCTs.

A dosimetric comparison was conducted to quantify the uncertainties introduced in dose calculation due to resampling. To evaluate resampling effects on structures of different densities, dose-volume histograms (DVH) were analyzed for the PTV, bone within the PTV, brain, liver, stomach, bowel and right and left lung. Upper ribs and lower ribs, divided at the lung basis, were also evaluated separately to assess the effect of abrupt changes in density of nearby tissues. For each structure, $D_{98\%}$, $D_{90\%}$, $D_{2\%}$, $V_{20\%}$ and $V_{30\%}$ values were compared between oCT and rCT using Wilcoxon signed rank tests.

Dose distribution comparisons between oCT and rCT were conducted using the gamma evaluation method implemented in PyMedPhys [25]. Three-dimensional gamma passing rates (GPR) were computed using a 1%(global)/1.25 mm criterion and a 20% dose threshold, considering the whole-body, PTV, bone within the PTV, brain, liver, right and left lung.

Six radiation oncologists (ROs) evaluated the clinical relevance and overall quality of the resampled images for diagnostics and contouring purposes of lymph nodes. The former examination covered the brain, lungs, liver, kidneys, bowel, and bone, while the latter assessment focused on the head and neck, thoracic, abdominal, and pelvic regions.

The evaluation involved rating in blind mode each oCT and rCT on a scale of 1 (poor) to 5 (optimal). To spot potential inconsistencies in the visual appearance of CT images, the evaluators could navigate through the entire CT series, zoom in, and apply window/level adjustments, but were restricted from switching between image types until completing each individual assessment. The evaluations concluded with oncologists determining whether the examined CT could be the oCT. In total, 300 evaluations (30 per patient) were conducted. A statistical analysis of the ratings was then performed using the Wilcoxon signed-rank test to detect significant differences between oCT and rCT images. The significance level was set to 0.05 throughout the whole study.

The overall workflow of the study is shown in Figure 2.

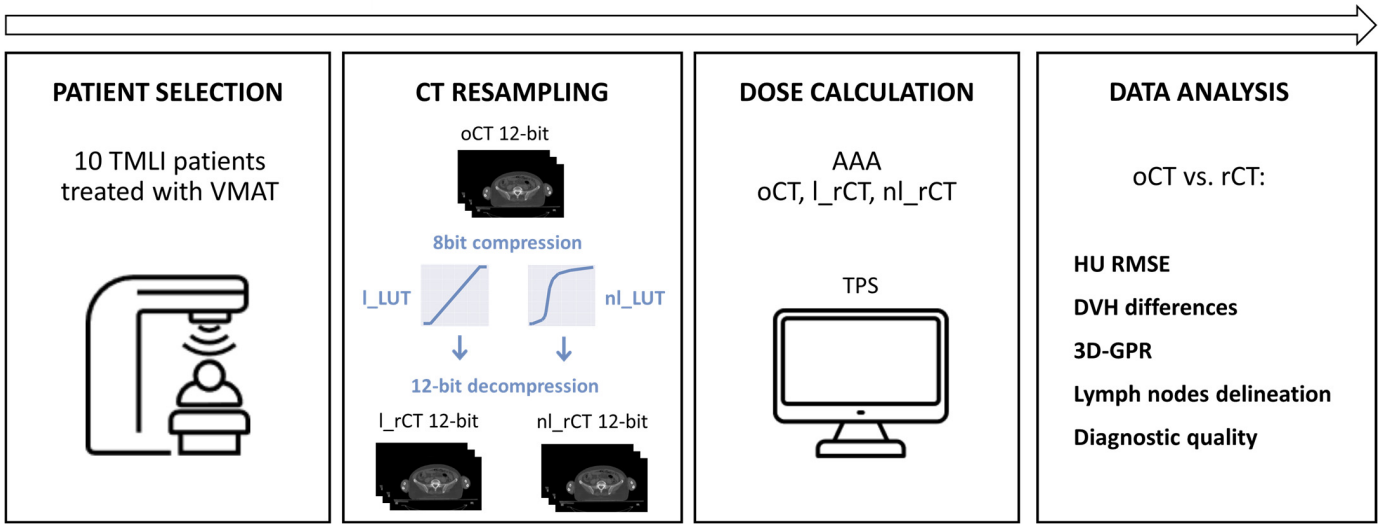

Figure 2. Overall workflow of this study. Abbreviations: AAA, analytical anisotropic algorithm; DVH, dose-volume histogram; GPR, gamma passing rate; HU, Hounsfield units; l_LUT, linear look-up table; l_rCT, linearly resampled CT; nl_LUT, non-linear look-up table; nl_rCT, non-linearly resampled CT; oCT, original CT; rCT, resampled CT; RMSE, root mean squared error; TMLI, total marrow and lymphoid irradiation.

3. Results

Among all patients, the HU comparison between oCT and rCT revealed a higher RMSE when using the nl_LUT rather than the l_LUT, with average and standard deviation of 10 ± 1 HU and 7 ± 1 HU, respectively. However, when restricted to voxels within the 0–100 HU range, the finer discretization of the nl_LUT yielded a much smaller RMSE of 0.70 ± 0.01 HU compared with 9.4 ± 0.1 HU of the l_LUT.

Figure 3 shows the DVH comparisons between oCT and rCT. Overall, resampling introduced minor hotspots, with nl_LUT producing smaller differences than l_LUT, except for the lungs, where nl_LUT yielded differences larger than l_LUT at lower doses, between 1.0 and 1.5 Gy. $D_{98\%}$, $D_{2\%}$, $D_{90\%}$, $V_{20\%}$ and $V_{30\%}$ statistics, reported in Table 2, showed median variations $\leq$0.4% in both the linear and non-linear case. In most cases, these resulted in statistical significance.

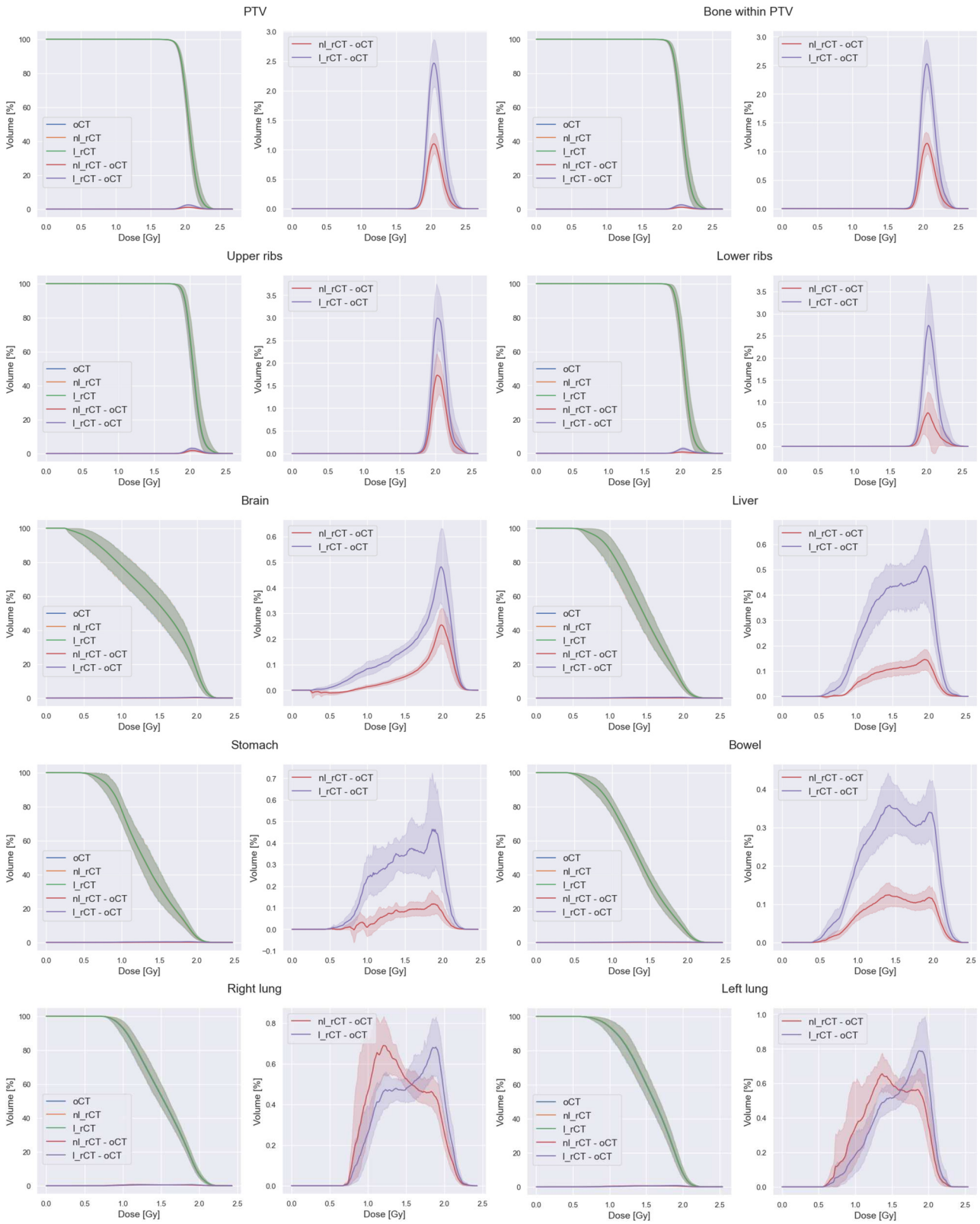

Figure 3. DVH comparison between oCT- and rCT-based plans for target volumes and OARs. The first and third columns show the population-averaged DVHs and the corresponding point-wise DVH differences, while the second and fourth columns display an enlarged view of the differences. The bands show the 95% CI across the cohort. Abbreviations: CI, confidence interval; l_rCT, linearly resampled CT; nl_rCT, non-linearly resampled CT; oCT, original CT.

Table 2. Median differences of $D_{98\%}$, $D_{90\%}$, $D_{2\%}$, $V_{20\%}$ and $V_{30\%}$ with interquartile range (IQR) for PTV, bone within the PTV, ribs, brain, liver, stomach, bowel, right and left lung. Column names refer to the plans being compared, i.e., "oAAA" stands for dose recalculated with AAA on oCT, while "l_r" and "nl_r" indicate l_rCTs and nl_rCTs, respectively.

Structure	DVH Statistic	Median Differences ± IQR [%]	
		l_rAAA-oAAA	nl_rAAA-oAAA
PTV	$D_{98\%}$	0.3 ± 0.1 *	0.1 ± 0.1 *
	$D_{90\%}$	0.3 ± 0.1 *	0.2 ± 0.1 *
	$D_{2\%}$	0.3 ± 0.2 *	0.1 ± 0.1 *
	$V_{20\%}$	0.0 ± 0.0	0.0 ± 0.0
	$V_{30\%}$	0.0 ± 0.0	0.0 ± 0.0
Bone within PTV	$D_{98\%}$	0.3 ± 0.1 *	0.1 ± 0.1 *
	$D_{90\%}$	0.3 ± 0.2 *	0.2 ± 0.1 *
	$D_{2\%}$	0.3 ± 0.1 *	0.2 ± 0.1 *
	$V_{20\%}$	0.0 ± 0.0	0.0 ± 0.0
	$V_{30\%}$	0.0 ± 0.0	0.0 ± 0.0
Upper Ribs	$D_{98\%}$	0.3 ± 0.0 *	0.2 ± 0.1 *
	$D_{90\%}$	0.3 ± 0.1 *	0.2 ± 0.1 *
	$D_{2\%}$	0.4 ± 0.1 *	0.2 ± 0.1 *
	$V_{20\%}$	0.0 ± 0.0	0.0 ± 0.0
	$V_{30\%}$	0.0 ± 0.0	0.0 ± 0.0
Lower Ribs	$D_{98\%}$	0.0 ± 0.1 *	0.0 ± 0.0 *
	$D_{90\%}$	0.4 ± 0.2 *	0.1 ± 0.0 *
	$D_{2\%}$	0.3 ± 0.2 *	0.1 ± 0.0 *
	$V_{20\%}$	0.0 ± 0.0	0.0 ± 0.0
	$V_{30\%}$	0.0 ± 0.0	0.0 ± 0.0
Brain	$D_{98\%}$	0.0 ± 0.1 *	0.0 ± 0.0
	$D_{90\%}$	0.1 ± 0.1 *	0.0 ± 0.0
	$D_{2\%}$	0.2 ± 0.0 *	0.1 ± 0.0 *
	$V_{20\%}$	0.0 ± 0.0	0.0 ± 0.1
	$V_{30\%}$	0.2 ± 0.2 *	−0.1 ± 0.1 *
Liver	$D_{98\%}$	0.2 ± 0.1 *	0.0 ± 0.1
	$D_{90\%}$	0.2 ± 0.1 *	0.0 ± 0.1
	$D_{2\%}$	0.3 ± 0.1 *	0.1 ± 0.0 *
	$V_{20\%}$	0.0 ± 0.0	0.0 ± 0.0
	$V_{30\%}$	0.0 ± 0.0	0.0 ± 0.0
Stomach	$D_{98\%}$	0.1 ± 0.1 *	0.0 ± 0.0
	$D_{90\%}$	0.1 ± 0.1 *	0.0 ± 0.0
	$D_{2\%}$	0.4 ± 0.1 *	0.1 ± 0.0 *
	$V_{20\%}$	0.0 ± 0.0	0.0 ± 0.0
	$V_{30\%}$	0.0 ± 0.2	0.0 ± 0.0
Bowel	$D_{98\%}$	0.1 ± 0.0 *	0.0 ± 0.0
	$D_{90\%}$	0.1 ± 0.0 *	0.0 ± 0.1
	$D_{2\%}$	0.4 ± 0.1 *	0.1 ± 0.0 *
	$V_{20\%}$	0.0 ± 0.0	0.0 ± 0.0
	$V_{30\%}$	0.3 ± 0.7 *	0.1 ± 0.2 *
Right lung	$D_{98\%}$	0.2 ± 0.1 *	0.4 ± 0.2 *
	$D_{90\%}$	0.3 ± 0.0 *	0.4 ± 0.1 *
	$D_{2\%}$	0.3 ± 0.0 *	0.2 ± 0.2 *
	$V_{20\%}$	0.0 ± 0.0	0.0 ± 0.0
	$V_{30\%}$	0.0 ± 0.0	0.0 ± 0.0
Left lung	$D_{98\%}$	0.3 ± 0.1 *	0.4 ± 0.1 *
	$D_{90\%}$	0.3 ± 0.1 *	0.4 ± 0.1 *
	$D_{2\%}$	0.3 ± 0.1 *	0.2 ± 0.1 *
	$V_{20\%}$	0.0 ± 0.0	0.0 ± 0.0
	$V_{30\%}$	0.0 ± 0.0	0.0 ± 0.0

* Significant differences. Abbreviations: AAA, analytical anisotropic algorithm; IQR, interquartile range; l_rCT, linearly resampled CT; nl_rCT, non-linearly resampled CT; oCT, original CT.

Figure 4 shows dose differences and 3D gamma index plots for a representative case, while Table 3 reports the median 3D-GPR obtained for all the comparisons. The 3D-GPRs revealed a nearly perfect agreement between dose distributions, both for whole-body and for each structure, with values equal to 100% in almost all cases.

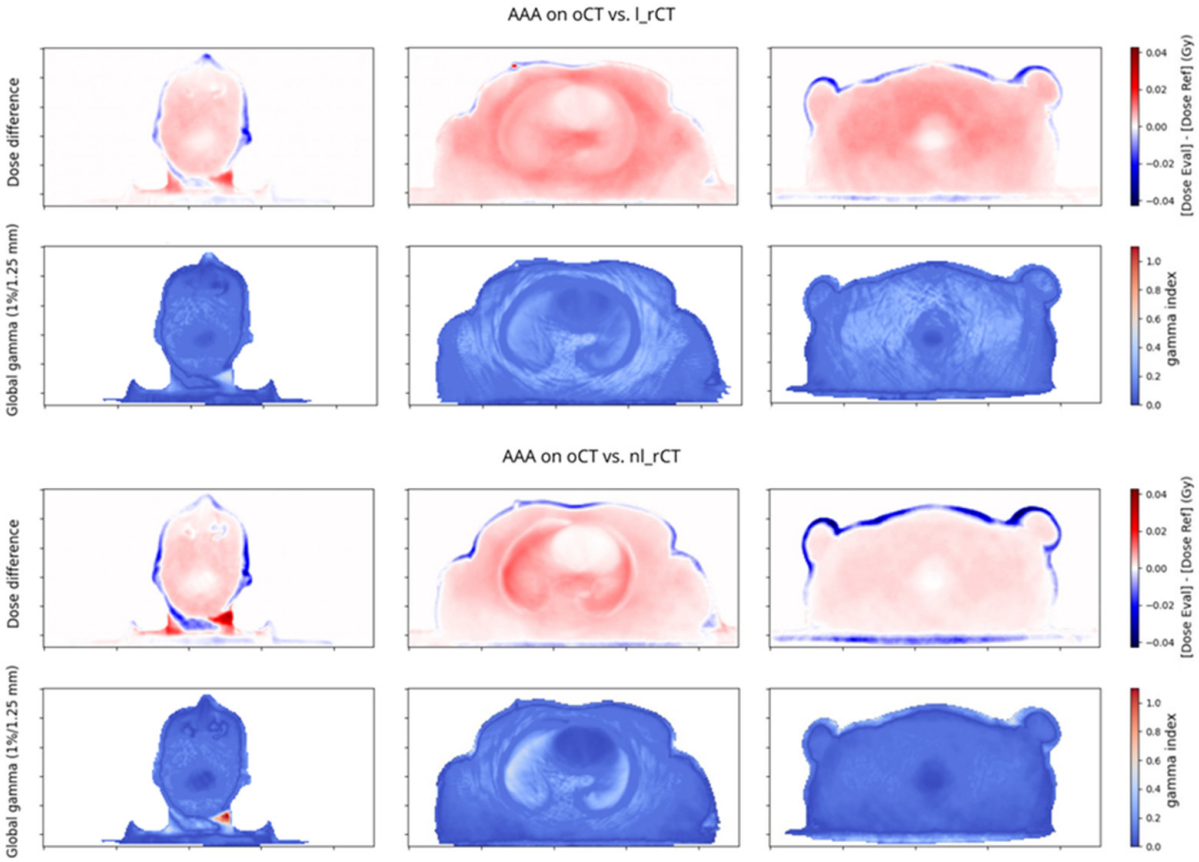

Figure 4. Dose distribution differences (first and third rows) and 3D gamma index maps (second and fourth rows) comparing l_rCT-based plans (upper panel) and nl_rCT-based plans (lower panel) with respect to the oCT-based plan. Three slices from head, lungs and pelvic regions of a representative case are shown. Abbreviations: AAA, analytical anisotropic algorithm; l_rCT, linearly resampled CT; nl_rCT, non-linearly resampled CT; oCT, original CT.

Table 3. Median and IQR values for 3D-GPRs. Column names refer to the plans being compared, i.e., "oAAA" stands for a plan recalculated with AAA on oCT, while "l_r" and "nl_r" indicate l_rCTs and nl_rCTs, respectively.

Volume	Median GPR ± IQR [%]	
	l_rAAA-oAAA	nl_rAAA-oAAA
Whole-body	100 ± 0	100.0 ± (<0.1)
PTV	100 ± 0	100 ± 0
Bone within PTV	100 ± 0	100 ± 0
Brain	100 ± 0	100 ± 0
Liver	100 ± 0	100 ± 0
Right lung	100 ± 0	100 ± 0
Left lung	100 ± 0	100 ± 0

Abbreviations: AAA, analytical anisotropic algorithm; IQR, interquartile range; l_rCT, linearly resampled CT; nl_rCT, non-linearly resampled CT; oCT, original CT.

Figure 5 presents original and resampled slices of the brain and lungs for a representative case. The l_rCTs exhibited noticeable pixelation in the brain, while the nl_rCTs showed

no observable differences from the oCT. Consequently, the median quality score assigned to the brain was 4 for both oCT (interquartile range—IQR = 1) and nl_rCT (IQR = 1), whereas it was 1 (IQR = 0) for l_rCT. Median scores for other anatomical regions consistently exceeded 4, including the head and neck for l_rCT, which, despite its suboptimal image quality, was still deemed usable for lymph nodes delineation. A significant difference was observed only between the scores of oCT vs. l_rCT for the brain ($p < 0.01$). The image quality scores across CTs and anatomical regions are reported in Table S1 of the Supplementary Material. Regarding the evaluation of whether the examined CT could be the oCT, two evaluations resulted in the rejection of all three images, while in all other cases, only the l_rCT received a negative response.

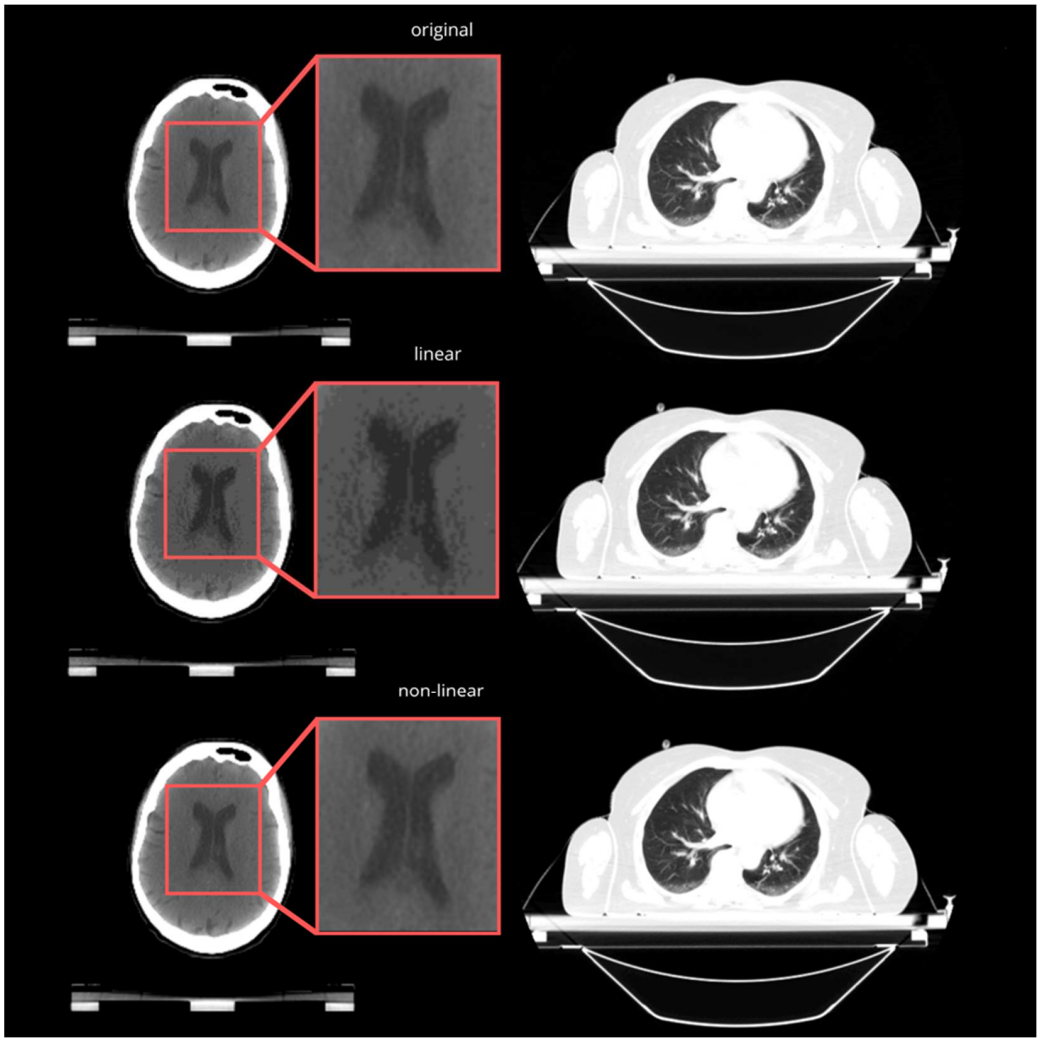

Figure 5. CT slices of the brain and lung regions from a representative patient, shown for oCT, l_rCT, and nl_rCT in the first, second, and third row, respectively. Compared with oCT and nl_rCT images, increased pixelation is observed in the brain region of the l_rCT images. Abbreviations: l_rCT, linearly resampled CT; nl_rCT, non-linearly resampled CT; oCT, original CT.

4. Discussion

In this study, we assessed the uncertainties in dose calculation and image quality introduced by a linear and a non-linear CT resampling process involving 12-bit to 8-bit compression and subsequent 8-bit to 12-bit decompression. Our goal was to evaluate the impact of the intermediate 8-bit compression step, which aligns with the standard channel depth used in common deep learning libraries and pre-trained models. This preliminary

assessment was necessary to determine whether the proposed non-linear method could be applied to sCT generation.

Our findings showed that only the nl_LUT, specifically designed to enhance HU representation in soft tissues, met the quality requirements for contouring and diagnostic applications, owing to its finer discretization step between 0–100 HU (see Table 1). Within this range, the nl_LUT demonstrated a clear improvement in image fidelity, with an RMSE of 0.70 ± 0.01 HU compared with 9.4 ± 0.1 HU of the l_LUT. However, the l_LUT yielded better global numerical accuracy, with a lower overall RMSE (7 ± 1 HU) than the nl_LUT (10 ± 1 HU), making it a viable alternative for dosimetric applications. Importantly, neither the l_LUT nor the nl_LUT introduced clinically relevant differences in dose calculation.

The nl_LUT slightly reduced numerical accuracy at the extremes of the HU scale (i.e., lung and bone), where its discretization step exceeded that of the l_LUT (100 HU vs. 16 HU). Nevertheless, DVH differences with the nl_LUT were consistently smaller than those observed with the l_LUT, including in organs influenced by adjacent air or bone structures, such as the stomach, bowel, and ribs. The lungs represented the only exception (see Figure 3 and Table 2). Despite this, no discernible differences in image quality were observed between oCTs and nl_rCTs in lung and bone regions, whereas l_rCTs proved inadequate for soft tissues reconstruction, particularly in the brain.

The 3D-GPR analysis did not reveal relevant dose discrepancies between oCTs and rCTs. To detect subtle differences introduced by resampling, we applied a stringent acceptance criterion of 1%/1.25 mm and a 20% dose threshold, enhancing sensitivity in high-dose regions. Given the large PTV in TMLI, encompassing approximately 20% of the body, this threshold effectively excluded only superficial regions near the skin, where dose calculation noise is more pronounced. The choice of 1.25 mm as the distance criterion was based on its correspondence to half the dose calculation grid size, ensuring appropriate sensitivity to spatial variations without introducing excessive noise from interpolation. Consequently, resampling-induced errors remained well below the 2–3% margin required to maintain the 5% accuracy threshold for absorbed dose estimation in the target volume [26,27]. Only a minor effect was observed in the neck region of the nl_rCT for the representative case reported in Figure 4, likely due to the combined presence of the immobilization system, adjacent bone structures, and air, as well as the adopted gamma criterion. Notably, the gamma analysis did not reveal relevant differences near the ribs, despite a similar tissue composition.

We also performed an additional analysis by recalculating treatment plans using a second clinical dose calculation algorithm (Acuros XB, AXB). The same dosimetric evaluation was repeated for AXB, and dose distributions calculated with AAA and AXB were compared on oCTs. Detailed methods and results are provided in Section S3 of the Supplementary Material. Overall, differences associated with the choice of dose calculation algorithm exceeded the uncertainties introduced by CT resampling [28–35].

This study has some limitations. Although whole-body CTs were analyzed to evaluate the impact of resampling across multiple anatomical regions, TMLI may tolerate relatively coarse errors due to its extensive treatment volumes and specific clinical goals. Moreover, the slice thickness and dose calculation grid adopted in this study may not be optimal for other treatments, thereby limiting the generalizability of the findings to conventional fractionated RT. According to our protocol, a slice thickness of 5 mm was used, which is appropriate for TMLI as it reduces noise over the extended scan length [36]. The dose calculation grid was set to 2.5 mm to accommodate the large computational volume, while the 3D-GPR was evaluated on a finer 1.25 mm grid via interpolation. Extending this analysis in other scenarios in which dose calculations are more sensitive to image fidelity, such as stereotactic body radiation therapy or proton therapy, would provide additional insights.

Future work should focus on optimizing the nl_LUT to further reduce errors in lung and bone regions while preserving fine discretization in soft tissues or tailoring the LUT to specific treatment sites. It is also essential to investigate the impact of the proposed nl_LUT on both output image quality and training performance in sCT generation models. This aspect will be addressed in a future study. Although the proposed nl_LUT improved image fidelity, it remains a hand-crafted solution and may have limited generalizability. Alternative approaches, such as embedding 8-bit compression directly within a neural network or employing dedicated deep learning-based compression models, could potentially achieve comparable results without relying on manually designed LUTs. Notably, Cao et al. compared linear and non-linear normalization methods for generating sCT images from megavoltage CBCTs of the head [16], demonstrating that different normalization strategies affect image quality across intensity ranges.

Finally, recent studies have explored the use of 16-bit CT representations to improve dose calculation accuracy in the presence of high-density materials, such as metal implants [37,38]. In our framework, 8-bit compression is an intermediate step for model development, and the proposed LUT strategy could be, in principle, also implemented with 16-bit depth CTs, enabling different trade-offs between compression rate and fidelity.

5. Conclusions

In this study, we investigated the impact of two CT resampling methods on dose calculation and image quality. These methods represent data processing steps required to ensure compatibility with deep learning libraries and pre-trained models designed for 8-bit images. By isolating the resampling process without introducing additional intermediate steps, we estimated the minimal error inherently associated with reconstructing CT images through an 8-bit deep learning workflow.

Dose calculation discrepancies were found to be clinically acceptable for both approaches, and the linear LUT provided adequate compression for dosimetric applications. In contrast, for diagnostic and contouring purposes, the proposed non-linear LUT improved image fidelity, particularly in soft tissue regions characterized by subtle density variations. Therefore, the non-linear LUT may represent an effective strategy for optimizing CT resampling in future AI-based applications for sCT generation when enhanced soft tissue representation is required.

Supplementary Materials: The following supporting information can be downloaded at: https://www.mdpi.com/article/10.3390/app16031660/s1.

Author Contributions: Conceptualization, D.L. and P.M.; Data curation, M.B.; Formal analysis, M.B.; Methodology, M.B., N.L. and P.M.; Resources, S.T., M.S., C.L. and P.M.; Supervision, P.M.; Visualization, M.B. and N.L.; Writing—original draft, M.B.; Writing—review & editing, N.L., D.L., S.T., M.S., C.L. and P.M. All authors have read and agreed to the published version of the manuscript.

Funding: This research received no external funding.

Institutional Review Board Statement: The study was conducted in accordance with the Declaration of Helsinki, and approved by the Institutional Ethics Committee of IRCCS Humanitas Research Hospital (ID 2928, 26 January 2021).

Informed Consent Statement: Informed consent was obtained from all subjects involved in the study.

Data Availability Statement: The data presented in this study are available on request from the corresponding author.

Conflicts of Interest: The authors declare no conflicts of interest.

Abbreviations

The following abbreviations are used in this manuscript:

AAA	Analytical anisotropic algorithm
AI	Artificial intelligence
CBCT	Cone beam computed tomography
CT	Computed tomography
CTV	Clinical target volume
DVH	Dose-volume histogram
GPR	Gamma passing rate
HU	Hounsfield unit
iMAR	Iterative metal artifact reduction
IQR	Interquartile range
LUT	Look-up table
l_LUT	Linear look-up table
MRI	Magnetic resonance imaging
nl_LUT	Non-linear look-up table
OAR	Organs at risk
oCT	Original computed tomography
PO	Photon optimization
PRO	Progressive resolution optimizer
PTV	Planning target volume
rCT	Resampled computed tomography
RMSE	Root mean squared error
RO	Radiation oncologist
RT	Radiation therapy
sCT	Synthetic computed tomography
TMLI	Total marrow and lymphoid irradiation
VMAT	Volumetric modulated arc therapy

References

1. Edmund, J.M.; Nyholm, T. A Review of Substitute CT Generation for MRI-Only Radiation Therapy. *Radiat. Oncol.* **2017**, *12*, 28. [CrossRef]
2. Schmidt, G.P.; Schoenberg, S.O.; Reiser, M.F.; Baur-Melnyk, A. Whole-Body MR Imaging of Bone Marrow. *Eur. J. Radiol.* **2005**, *55*, 33–40. [CrossRef]
3. Khoo, V.S.; Joon, D.L. New Developments in MRI for Target Volume Delineation in Radiotherapy. *Br. J. Radiol.* **2006**, *79*, S2–S15. [CrossRef]
4. Thummerer, A.; van der Bijl, E.; Galapon, A.J.; Kamp, F.; Savenije, M.; Muijs, C.; Aluwini, S.; Steenbakkers, R.J.H.M.; Beuel, S.; Intven, M.P.W.; et al. SynthRAD2025 Grand Challenge dataset: Generating synthetic CTs for radiotherapy from head to abdomen. *Med. Phys.* **2025**, *52*, e17981. [CrossRef] [PubMed]
5. Lavrova, E.; Garrett, M.D.; Wang, Y.-F.; Chin, C.; Elliston, C.; Savacool, M.; Price, M.; Kachnic, L.A.; Horowitz, D.P. Adaptive Radiation Therapy: A Review of CT-Based Techniques. *Radiol. Imaging Cancer* **2023**, *5*, e230011. [CrossRef]
6. Boulanger, M.; Nunes, J.-C.; Chourak, H.; Largent, A.; Tahri, S.; Acosta, O.; De Crevoisier, R.; Lafond, C.; Barateau, A. Deep Learning Methods to Generate Synthetic CT from MRI in Radiotherapy: A Literature Review. *Phys. Medica* **2021**, *89*, 265–281. [CrossRef]
7. Spadea, M.F.; Maspero, M.; Zaffino, P.; Seco, J. Deep Learning Based Synthetic-CT Generation in Radiotherapy and PET: A Review. *Med. Phys.* **2021**, *48*, 6537–6566. [CrossRef]
8. Vera-Olmos, J.; Torrado-Carvajal, A.; Prieto-de-la-Lastra, C.; Catalano, O.A.; Rozenholc, Y.; Mazzeo, F.; Soricelli, A.; Salvatore, M.; Izquierdo-Garcia, D.; Malpica, N. How to Pseudo-CT: A Comparative Review of Deep Convolutional Neural Network Architectures for CT Synthesis. *Appl. Sci.* **2022**, *12*, 11600. [CrossRef]
9. Vellini, L.; Zucca, S.; Lenkowicz, J.; Menna, S.; Catucci, F.; Quaranta, F.; Pilloni, E.; D'Aviero, A.; Aquilano, M.; Di Dio, C.; et al. A Deep Learning Approach for the Fast Generation of Synthetic Computed Tomography from Low-Dose Cone Beam Computed Tomography Images on a Linear Accelerator Equipped with Artificial Intelligence. *Appl. Sci.* **2024**, *14*, 4844. [CrossRef]

10. Pan, S.; Abouei, E.; Wynne, J.; Chang, C.-W.; Wang, T.; Qiu, R.L.J.; Li, Y.; Peng, J.; Roper, J.; Patel, P.; et al. Synthetic CT Generation from MRI Using 3D Transformer-Based Denoising Diffusion Model. *Med. Phys.* **2024**, *51*, 2538–2548. [CrossRef] [PubMed]
11. Dahiya, N.; Alam, S.R.; Zhang, P.; Zhang, S.-Y.; Li, T.; Yezzi, A.; Nadeem, S. Multitask 3D CBCT-to-CT Translation and Organs-at-Risk Segmentation Using Physics-Based Data Augmentation. *Med. Phys.* **2021**, *48*, 5130–5141. [CrossRef]
12. Klaser, K.; Borges, P.; Shaw, R.; Ranzini, M.; Modat, M.; Atkinson, D.; Thielemans, K.; Hutton, B.; Goh, V.; Cook, G.; et al. A Multi-Channel Uncertainty-Aware Multi-Resolution Network for MR to CT Synthesis. *Appl. Sci.* **2021**, *11*, 1667. [CrossRef]
13. Karimzadeh, M.; Seyedarabi, H.; Jodeiri, A.; Afrouzian, R. Enhanced Brain Stroke Lesion Segmentation in MRI Using a 2.5D Transformer Backbone U-Net Model. *Brain Sci.* **2025**, *15*, 778. [CrossRef]
14. Usama, Z.; Alavi, A.; Chan, J. A Review on the Applications of GANs for 3D Medical Image Analysis. *Appl. Sci.* **2025**, *15*, 11219. [CrossRef]
15. Marcel, S.; Rodriguez, Y. Torchvision the Machine-Vision Package of Torch. In Proceedings of the 18th ACM International Conference on Multimedia, Firenze, Italy, 25–29 October 2010; ACM: New York, NY, USA, 2010; pp. 1485–1488.
16. Cao, Z.; Gao, X.; Chang, Y.; Liu, G.; Pei, Y. Improving Synthetic CT Accuracy by Combining the Benefits of Multiple Normalized Preprocesses. *J. Appl. Clin. Med. Phys.* **2023**, *24*, e14004. [CrossRef]
17. Mancosu, P.; Navarria, P.; Muren, L.P.; Castagna, L.; Reggiori, G.; Clerici, E.; Sarina, B.; Bramanti, S.; De Philippis, C.; Tomatis, S.; et al. Development of an Immobilization Device for Total Marrow Irradiation. *Pract. Radiat. Oncol.* **2021**, *11*, e98–e105. [CrossRef]
18. Bär, E.; Schwahofer, A.; Kuchenbecker, S.; Häring, P. Improving Radiotherapy Planning in Patients with Metallic Implants Using the Iterative Metal Artifact Reduction (iMAR) Algorithm. *Biomed. Phys. Eng. Express* **2015**, *1*, 025206. [CrossRef]
19. Dei, D.; Lambri, N.; Stefanini, S.; Vernier, V.; Brioso, R.C.; Crespi, L.; Clerici, E.; Bellu, L.; De Philippis, C.; Loiacono, D.; et al. Internal Guidelines for Reducing Lymph Node Contour Variability in Total Marrow and Lymph Node Irradiation. *Cancers* **2023**, *15*, 1536. [CrossRef]
20. Mancosu, P.; Navarria, P.; Castagna, L.; Roggio, A.; Pellegrini, C.; Reggiori, G.; Fogliata, A.; Lobefalo, F.; Castiglioni, S.; Alongi, F.; et al. Anatomy Driven Optimization Strategy for Total Marrow Irradiation with a Volumetric Modulated Arc Therapy Technique. *J. Appl. Clin. Med. Phys.* **2012**, *13*, 138–147. [CrossRef]
21. Cressoni, M.; Gallazzi, E.; Chiurazzi, C.; Marino, A.; Brioni, M.; Menga, F.; Cigada, I.; Amini, M.; Lemos, A.; Lazzerini, M.; et al. Limits of Normality of Quantitative Thoracic CT Analysis. *Crit Care* **2013**, *17*, R93. [CrossRef]
22. DenOtter, T.D.; Schubert, J. Hounsfield Unit. In *StatPearls*; StatPearls Publishing: Treasure Island, FL, USA, 2025.
23. Kim, H.; Kim, G.; Yoon, B.C.; Kim, K.; Kim, B.-J.; Choi, Y.H.; Czosnyka, M.; Oh, B.-M.; Kim, D.-J. Quantitative Analysis of Computed Tomography Images and Early Detection of Cerebral Edema for Pediatric Traumatic Brain Injury Patients: Retrospective Study. *BMC Med.* **2014**, *12*, 186. [CrossRef]
24. Lamba, R.; McGahan, J.P.; Corwin, M.T.; Li, C.-S.; Tran, T.; Seibert, J.A.; Boone, J.M. CT Hounsfield Numbers of Soft Tissues on Unenhanced Abdominal CT Scans: Variability Between Two Different Manufacturers' MDCT Scanners. *Am. J. Roentgenol.* **2014**, *203*, 1013–1020. [CrossRef]
25. Biggs, S.; Jennings, M.; Swerdloff, S.; Chlap, P.; Lane, D.; Rembish, J.; McAloney, J.; King, P.; Ayala, R.; Guan, F.; et al. PyMedPhys: A Community Effort to Develop an Open, Python-Based Standard Library for Medical Physics Applications. *J. Open Source Softw.* **2022**, *7*, 4555. [CrossRef]
26. ICRU Reports. Reports of the International Commission on Radiation Units and Measurements. *J. ICRU* **1976**, *os-13*, 63–65. [CrossRef]
27. Papanikolaou, N.; Battista, J.J.; Boyer, A.L.; Kappas, C.; Klein, E.; Mackie, T.R.; Sharpe, M.; Dyk, J.V. *Tissue Inhomogeneity Corrections for Megavoltage Photon Beams*; AAPM: Alexandria, VA, USA, 2004.
28. Takizawa, T.; Tanabe, S.; Utsunomiya, S.; Nakano, H.; Yamada, T.; Sakai, H.; Ohta, A.; Saito, H.; Nakano, T.; Abe, E.; et al. Dosimetric Comparison of Analytic Anisotropic Algorithm and Acuros XB Algorithm in VMAT Plans for High-Grade Glioma. *Phys. Med.* **2020**, *73*, 73–82. [CrossRef]
29. Kan, M.W.K.; Leung, L.H.T.; Yu, P.K.N. Dosimetric Impact of Using the Acuros XB Algorithm for Intensity Modulated Radiation Therapy and RapidArc Planning in Nasopharyngeal Carcinomas. *Int. J. Radiat. Oncol.* **2013**, *85*, e73–e80. [CrossRef]
30. Zhen, H.; Hrycushko, B.; Lee, H.; Timmerman, R.; Pompoš, A.; Stojadinovic, S.; Foster, R.; Jiang, S.B.; Solberg, T.; Gu, X. Dosimetric Comparison of Acuros XB with Collapsed Cone Convolution/Superposition and Anisotropic Analytic Algorithm for Stereotactic Ablative Radiotherapy of Thoracic Spinal Metastases. *J. Appl. Clin. Med. Phys.* **2015**, *16*, 181–192. [CrossRef]
31. Hirashima, H.; Nakamura, M.; Nakamura, K.; Matsuo, Y.; Mizowaki, T. Dosimetric Verification of Four Dose Calculation Algorithms for Spine Stereotactic Body Radiotherapy. *J. Radiat. Res.* **2024**, *65*, 109–118. [CrossRef]
32. Hirata, K.; Nakamura, M.; Yoshimura, M.; Mukumoto, N.; Nakata, M.; Ito, H.; Inokuchi, H.; Matsuo, Y.; Mizowaki, T.; Hiraoka, M. Dosimetric Evaluation of the Acuros XB Algorithm for a 4 MV Photon Beam in Head and Neck Intensity-Modulated Radiation Therapy. *J. Appl. Clin. Med. Phys.* **2015**, *16*, 52–64. [CrossRef]
33. Alhakeem, E.A.; AlShaikh, S.; Rosenfeld, A.B.; Zavgorodni, S.F. Comparative Evaluation of Modern Dosimetry Techniques near Low- and High-Density Heterogeneities. *J. Appl. Clin. Med. Phys.* **2015**, *16*, 142–158. [CrossRef]

34. Fogliata, A.; Nicolini, G.; Clivio, A.; Vanetti, E.; Cozzi, L. On the Dosimetric Impact of Inhomogeneity Management in the Acuros XB Algorithm for Breast Treatment. *Radiat. Oncol.* **2011**, *6*, 103. [CrossRef]
35. Fogliata, A.; Nicolini, G.; Clivio, A.; Vanetti, E.; Cozzi, L. Dosimetric Evaluation of Acuros XB Advanced Dose Calculation Algorithm in Heterogeneous Media. *Radiat. Oncol.* **2011**, *6*, 82. [CrossRef]
36. Parsons, D.; Lim, T.Y.; Teruel, J.R.; Galavis, P.; Agostinelli, S.; Liang, J.; Mancosu, P.; Cherpak, A.; Stanley, D.N.; Ahn, K.-H.; et al. Considerations for Intensity Modulated Total Body or Total Marrow and Lymphoid Irradiation. *Clin. Transl. Radiat. Oncol.* **2023**, *43*, 100674. [CrossRef]
37. Abdul Aziz, M.Z.; Ali, M.H.; Jayamani, J.; Osman, N.D.; Salehi, Z.; Tajuddin, A.A. Determination of Computed Tomography Number of High-Density Materials in 12-Bit, 12-Bit Extended and 16-Bit Depth for Dosimetric Calculation in Treatment Planning System. *J. Radiother. Pract.* **2019**, *18*, 285–294. [CrossRef]
38. Gao, L.; Sun, H.; Ni, X.; Fang, M.; Lin, T. Effects of 16-Bit CT Imaging Scanning Conditions for Metal Implants on Radiotherapy Dose Distribution. *Oncol. Lett.* **2018**, *15*, 2373–2379. [CrossRef]

Disclaimer/Publisher's Note: The statements, opinions and data contained in all publications are solely those of the individual author(s) and contributor(s) and not of MDPI and/or the editor(s). MDPI and/or the editor(s) disclaim responsibility for any injury to people or property resulting from any ideas, methods, instructions or products referred to in the content.